Uniform light delivery in volumetric optoacoustic tomography

Ben Mc Larney[1,2,¶], Johannes Rebling[1,2,3,4¶], Zhenyue Chen[1], Xosé Luis Deán-Ben[1,3,4], Sven Gottschalk[1] & Daniel Razansky[1,2,3,4*]

[1]Institute for Biological and Medical Imaging, Helmholtz Center Munich, Neuherberg, Germany

[2]Faculty of Medicine, Technical University of Munich, Germany

[3]Faculty of Medicine and Institute of Pharmacology and Toxicology, University of Zurich, Switzerland

[4]Institute for Biomedical Engineering and Department of Information Technology and Electrical Engineering, ETH Zurich, Switzerland

[*]Corresponding Author: E-mail: daniel.razansky@uzh.ch

[¶] Contributed equally

ABSTRACT

Accurate image reconstruction in volumetric optoacoustic tomography implies the efficient generation and collection of ultrasound signals around the imaged object. Non-uniform delivery of the excitation light is a common problem in optoacoustic imaging often leading to a diminished field of view, limited dynamic range and penetration, as well as impaired quantification abilities. Presented here is an optimised illumination concept for volumetric tomography that utilizes additive manufacturing via 3D printing in combination with custom-made optical fiber illumination. The custom-designed sample chamber ensures convenient access to the imaged object along with accurate positioning of the sample and a matrix array ultrasound transducer used for collection of the volumetric image data. Raytracing is employed to optimize the positioning of the individual fibers in the chamber. Homogeneity of the generated light excitation field was confirmed in tissue-mimicking agar spheres. Applicability of the system to image entire mouse organs *ex vivo* has been showcased. The new approach showed a clear advantage over conventional, single-sided illumination strategies by eliminating the need to correct for illumination variances and resulting in

This article has been accepted for publication and undergone full peer review but has not been through the copyediting, typesetting, pagination and proofreading process, which may lead to differences between this version and the Version of Record. Please cite this article as doi: 10.1002/jbio.201800387

enhancement of the effective field of view, greater penetration depth and significant improvements in the overall image quality.

Keywords: optoacoustics, 3d-printing, organs, imaging, illumination, fibers

1. INTRODUCTION

In optoacoustic (OA) imaging and tomography, tissue contrast arises from the absorption of intermittent (pulsed) light that is transformed into a broadband ultrasound wave field. There are many advantages in this technique over conventional imaging methods such as MRI and ultrasound. Examples of such advantages are improved contrast along with higher spatiotemporal resolution and the ability to select for and quantify separate biological components based on their light absorption.[1,2] Numerous embodiments have been suggested for OA imaging of areas located at depths ranging from superficial layers to centimetres within biological tissues.[3,4,5,6] In all implementations, the optimal illumination strategy implies confining the excitation light to the region of interest while avoiding light exposure levels that may cause cell toxicity or other damage to the imaged tissues.[7,8] For depths beyond the ballistic regime of light (~1 mm in biological tissues), image formation relies on acoustic image reconstruction methods. Light pulses in the millijoule range are typically required to achieve at least several millimetres of imaging depth in the near-infrared spectral window without employing extensive signal averaging.[9] Real-time 2D and 3D imaging can then be achieved via parallel acquisition of signals by means of ultrasound (US) arrays.[2, 10]

At present, curved US arrays employing cylindrically-focused or spherical matrix geometries are fostering the clinical translation of this technology by combining powerful real-time hand-held imaging capabilities with highly compelling image quality. [11,12,13,14,15,16, 17]

The unique advantages of the curved array technology for optimal collection of high quality OA tomographic data have also been exploited in many applications involving small animals. For example, hemodynamic changes in the entire brain of rodents have been mapped via single-wavelength and multi-spectral light excitation.[17,18,19] By delivering light with pulse repetition frequencies of hundreds or thousands of Hertz, it was possible to accurately track the motion of freely-swimming zebrafish larvae in 3D.[20,21] Imaging of isolated brains of adult zebrafish has further revealed neural activity patterns by capturing absorption changes of genetically encoded calcium indicators.[22]

To this end, several experimental and algorithmic strategies have been attempted in order to mitigate image artefacts related to sub-optimal object illumination. [23,24,25, 26,27,28] Here we introduce an optimized design for light delivery in three-dimensional optoacoustic tomography based on the combination of a custom-made optical fiber bundle with a 3D-printed (fused deposition modelling: FDM) sample chamber providing homogenous sample illumination.

2. MATERIALS AND METHODS

2.1. Fiber Bundle Light Delivery

The proposed design is based on an in-house fabricated optical fiber bundle. This bundle allows a more flexible and cost-effective light guiding approach in comparison to commonly-used bundles comprised of thousands of small multi-mode fibers with fused end-facets. Homogenous light delivery to the imaging target is achieved with a few, large core, step-index multimode fibers. The optimum number and arrangement of the individual fibers to provide uniform illumination on a spherical surface with 10 mm diameter were determined with ray tracing simulations performed in TracePro (version 7.3, Lambda Research Corporation, USA). The simulations included the fiber's characteristics (numerical aperture

(NA), core diameter) as well as the geometrical constraints posed by the transducer array's geometry and accessibility for sample placement. The estimated optimal arrangement of seven fibers is shown (**Figure 1a) and b)**). This arrangement is based on simulation results of the detector geometries and possible fiber placement around the detector (**Supplementary Figure 1**). The distal ends of the individual fibers were arranged in three groups with respect to the spherical array (**Supplementary Figure 2)**. The first group consisted of a single fiber illuminating the sample from below through an aperture in the transducer. A further two groups comprised of three fibers each were positioned above and around the sample with equal azimuthal separation of 120°. The lower three fibers were positioned at an elevational angle of 5.7° with respect to the horizontal plane while the second group was set at a steeper angle of 37°. Both groups were rotated in the azimuthal direction by 60° with respect to each other (see Supplementary Figure 2).

The specifications of the fibers used in the proposed design are summarized in Table S1. The bundle is comprised of seven multimode step-index fibers, each with a 600 µm core diameter (FT600EMT, Thorlabs, USA) and with a total length of approximately 1.5 m. These fibers offer a broad transmission bandwidth (400 to 2200 nm). Their Technology Enhanced Clad Silica (TECS) cladding makes them particularly mechanically robust, further providing improved bending performance and a large NA of 0.39 for efficient coupling of the excitation light at a reduced cost in comparison to conventional silica-clad fibers.[29] The individual fibers were stripped of their coating to increase the fill-factor at the coupling facet (i.e. the percentage area of the proximal end of the fiber into which light can be coupled which is the total area of fiber cores divided by the sum of fiber cores). They were bundled and connectorized to a conventional SMA905 multi-mode fiber connector (11580A, Thorlabs, USA). The connector's central bore was drilled to a size of 2 mm to accommodate the circularly packed fibers, which were glued in place using high-temperature epoxy

(353NDPK, Thorlabs, USA). The fiber end facets were polished to optical quality using a conventional fiber polishing procedure with a final grit size of 0.3 µm.[30] The resulting proximal end-facet is shown in Figure 1a). The separate fibers were then additionally protected using a reinforced jacket (FT020, Thorlabs, USA) and the individual, sensitive glass end-facets of the distal end were cleaved and protected using small steel ferrules. The fiber core diameter of 600 µm provides a good mechanical stability while keeping the fibers sufficiently flexible for handling and alignment. Using only seven fibers results in a bundle with sufficient light transmission (64% theoretical transmission) yet making its assembly, handling and alignment at the distal end more straightforward than for bundles with a larger number of fibers.

2.2. 3D Printed Sample Chamber

A watertight sample chamber for mounting the US transducer array, the optical fibers and the imaged sample was designed and manufactured accounting for mechanical constraints as well as for the optimum fiber positioning, as previously described. The base of the sample chamber is a cylinder having the diameter of the US transducer array casing and with watertight double O-ring seals between the chamber and the transducer (Figure 1 c)). The sample chamber has further openings through which separate 3D-printed fiber mounts were inserted under the previously determined optimal angles. The imaged samples were placed in the FOV of the transducer on a thin polyethylene film clamped on a 3D- printed ring mount. This film allowed unobstructed propagation of the OA signals toward the US transducer active surface whilst holding the sample in place (Figure 1 c)).

The separately designed fiber mounts (Figure 1b) and Supplementary Figure 2) enable a watertight, adjustable and interchangeable fixation for the individual fiber ends. They are comprised of a central cylinder with a rubber sealing and an external M10 thread onto which

a 3D-printed locking nut for a watertight fixation of the mount to the sample chamber is placed. The fibers protrude through a central hole in the fiber mount where they were fixed near the end with an M4 plastic set-screw (not shown). The end of the mount facing the sample additionally features three set-screws for fine-alignment of the fiber position. These fine-alignment screws were used prior to the imaging experiments to ensure a homogenous illumination of the sample in the FOV of the US transducer array.

Computer aided design (CAD) was performed using Inventor Professional 2017 (Autodesk, USA). All 3D-printing was carried out in house using two separate FDM 3D-printers. The sample chamber was manufactured using a RF1000 3D-printer (Renkforce, Germany) with a large 0.6 mm nozzle. The large nozzle diameter results in fast printing speeds with improved mechanical strength. The smaller parts, such as the fiber and sample mounts and the locking nuts were printed using an Ultimaker 2+ 3D-printer (Ultimaker, Netherlands) with a 0.2 mm nozzle diameter. This small nozzle provided the required accuracy for these small parts. All parts were prepared for printing using Simplify3D 3.0 software (Simplify3D, USA). The threads on the fiber mounts and in the locking nuts were cut in the 3D-printed parts using conventional metal taps and dies.

2.3. Volumetric Optoacoustic Tomography

A detailed description of the optoacoustic signal acquisition protocol is available elsewhere and is briefly summarized here for the sake of completeness. [31] The spherical matrix array transducer consists of 512 circular individual detection elements having a diameter of 2.5 mm and >80% detection bandwidth around a central frequency of 5 MHz (Imasonic SaS, Voray, France). The elements are distributed along a spherical surface with a 40 mm radius and 140° of angular coverage (1.31π solid angle). The OA signals captured by all the array elements were simultaneously digitized at 40 megasamples per second with a custom-made 512-

channel data acquisition unit (Falkenstein Mikrosysteme GmbH, Germany). Optical excitation was provided with an optical parametric oscillator (OPO)-based laser (SpitLight, Innolas Laser GmbH, Germany), whose Q-switch output was also used for triggering the signal acquisition. The laser beam was coupled into the proximal end (Figure 1a)) of the custom-made fiber bundle using an aspheric lens (f=50 mm, AL2550M, Thorlabs, USA). The fiber mounts were secured in the sample chamber and the individual fiber-ends were adjusted and fixed in place for optimal illumination. The US transducer array was placed at the bottom of the sample chamber and the chamber was filled with water to ensure acoustic coupling between the sample and transducer. For single sided illumination only the fiber marked located within the detector was used (yellow arrow in Figure 1a)). The laser was tuned to a wavelength of 532nm for sphere phantom imaging, a highly absorbing wavelength for blood and commonly used for phantom testing in OA tomography.[32,33,33] Excitation wavelength of 590nm was used for both heart and brain imaging as it has been previously shown to attain high contrast for elucidating organ structures.[6] The laser was operated at a pulse repetition frequency (PRF) of 10 Hz. The total per-pulse energy at the output of the fiber bundle was measured as 7.7 mJ (~1.1mJ per fiber, 48% coupling efficiency). Visualization in real-time during data acquisition was enabled by a graphics processing unit (GPU) implementation of a back-projection formula.[34]

2.4. Phantom Preparation and Imaging

Illumination uniformity with the proposed design was first tested by imaging a spherical, tissue-mimicking agar phantom. This phantom was designed to mimic highly absorbing biological tissue over a broad range of visible wavelengths in order to easily determine the uniformity of the illumination across the surface of the sphere. For this, an agar solution (1.5% agar powder dissolved in distilled water, 30391049, ThermoFisher Scientific, USA) was mixed to contain a final concentration of 6% Intralipid from a 20% emulsion (68890-65-

3, SigmaAldrich, USA) to mimic highly scattering tissue with reduced scattering coefficient μ'_s~10 cm^{-1}.[33] Black India ink (Higgins Ink, USA) with an optical absorption coefficient of μ_a~4 cm^{-1} was further added to the agar solution to simulate absorption of blood in the visible range.[32] This liquid solution was injected into a custom-made spherical polyvinyl chloride (PVC) mold. The solidified spherical phantom was then removed from the mold, placed in the sample chamber and imaged as described above.

The resolution of the system was tested by randomly embedding ~90μm diameter spheres (BKPMS-1.2 90-106um, Black Paramagnetic Polyethylene Microspheres, Cospheric, USA) in a cylindrical phantom with 16 mm diameter consisting of 1.5% agar dissolved in distilled water (30391049, ThermoFisher Scientific, USA). The microspheres were mainly distributed across a cross-section of the phantom, which was placed in the center of detector's FOV of scanned along the axial direction with 0.5 mm step. Imaging was performed at 532 nm. The resolution was estimated as the mean square difference between the measured full width at half maximum (FWHM) of a microsphere and its diameter. Note that the measured FWHM may be affected by negative values in the images associated to limited view effects, particularly along the z direction.[35] Thereby, the actual resolution of the system can be slightly lower.

2.5. Numerical Simulation

A numerical simulation was performed in order to facilitate interpretation of the obtained experimental results in tissue phantoms. For this, optoacoustic images corresponding to a uniformly illuminated sphere with the same optical properties as the one used in the experiments were reconstructed. The light fluence distribution within the sphere was estimated considering the light diffusion approximation using a constant fluence on the

surface of the sphere as a boundary condition. Under these assumptions, the light fluence distribution is described by a modified spherical Bessel function given by:

$$U(r) = \frac{U_0}{\frac{\sinh(kR)}{kR}} \times \frac{\sinh(kr)}{kr} \quad (1)$$

where U_0 is the fluence at the surface of the sphere, r is the distance from the center of the sphere with radius R. The photon diffusion wavenumber is defined as $k = \sqrt{\mu_a/D}$, where the photon diffusion coefficient $D = 1/3(\mu_a + \mu'_s)$ and μ_a and μ'_s are the absorption and reduced scattering coefficients, respectively. Considering a uniform absorption coefficient and a uniform Grüneisen parameter, the spatial distribution of the initial optoacoustic pressure is equivalent to that of the light fluence. The optoacoustic signals were then estimated with a discretized version of the time-domain optoacoustic model.[36] Note that limited-view effects are expected to affect the reconstructed images for the angular coverage of the array (140°), so that a reconstructed uniform sphere is not expected. The detection array was modelled by splitting its 140° spherical aperture into 512 individual elements, 2.5 mm diameter each. The effects of the finite aperture of the transducer elements (~2.5 mm in diameter) was accounted for by segmenting the surface of each element into 150 sub-elements and summing up the individual signals across the element.[37]

The simulated datasets were reconstructed using a model-based reconstruction iterative method, as reported elsewhere.[36] Prior to reconstruction, the signals were band-pass filtered between 0.1 - 6 MHz. Note that the model used for the tomographic reconstruction was also used as a forward model for simulations, but filtering prevents the inverse crime. The experimental signals were further deconvolved with the impulse response of the transducer. All reconstructions were performed on a 15x15x15 mm^3 3D Cartesian grid consisting of 150x150x150 voxels.

2.6. Biological Tissues Imaging

The system's performance was further demonstrated in actual biological samples by imaging a murine heart and brain *ex vivo*.

2.6.1 Brain Imaging

The brain was extracted from a female wild type CD1 mouse (approx. 10 weeks old). The mouse was euthanized using a lethal dose of Ketamine/Xylazine. Once euthanasia was completed, an incision was made along the *lina alba* for the length of the *peritoneum*. The chest cavity was opened and the mouse was perfused with artificial cerebrospinal fluid (ACSF) via insertion of a needle into the left ventricle. The right ventricle of the heart was then cut to allow fluid to flow out. Perfusion was carried out until the liver turned white, indicating complete blood removal. The solution was then changed to high sucrose-containing ACSF for further perfusion and finally to paraformaldehyde (PFA).[38] Next, the head was removed via decapitation. After removal of the skull, the brain was isolated and stored in high sucrose ACSF. Due to the orientation of the brain within the skull cavity a portion of the olfactory bulbs detached from the structure, and hence is reduced in size in comparison to a secondary brain which is shown in **Supplementary Figure 3**. The brain was then quick frozen and stored at -80°C, with the sucrose preventing the formation of ice crystals. Prior to the imaging experiment, the brain was defrosted and imaged at room temperature.

2.6.2 Heart Imaging

For heart isolation, a mouse with the same characteristics as described in 2.5.1 was euthanized. Once euthanasia was completed, the chest cavity was opened and the heart extracted. Excess fatty tissue around the heart was cut away. The heart was placed in PBS buffer until it stopped beating, so that any remaining blood in the heart was removed. The

heart was then placed into PFA for fixation. Imaging was then carried out in PBS at room temperature.

3. RESULTS

3.1. Phantom Imaging

The maximum intensity projections (MIPs) of the reconstructed optoacoustic images from a scattering and absorbing sphere phantom are shown in **Figure 2**. The top row displays projections along the z-axis (see Figure 2) while the second row shows side-views with projections along the y-axis. The third row shows single x-y slices through the sphere at a depth of 5 mm from the surface. The normalised maximum intensity for each z slice (circumference) of the respective sphere is shown in j). Automated code was implemented to fit a circle to the circumference and plot its corresponding maximum signal intensity. Clearly, only part of the hemisphere facing the illuminating bundle is visible in the images obtained with single-sided illumination (Figure 2a), d) and g)). In this case, the image quality is flawed by the excessive dispersion of optoacoustic signal magnitude, whereas the intensity values decay rapidly with increasing distance from the fiber (Figure 2a), d), g) and j), blue line) resulting in a "dark side of the moon" effect. The corresponding images obtained for the uniformly illuminated sphere are shown (Figure 2 b), e) and h)). Here, pressure waves are generated equally along the entire sphere surface since the illumination is evenly distributed across the object (Figure 2j), green line). The signal intensity at the top side of the sphere (z ~ 8 mm), corresponding to the most distant area from the transducer, is approximately 75% of the maximum. In comparison, the reconstructed image for single side illumination has a signal intensity at this position of less than 5% of the maximum (Figure 2j)). Moreover, the images reconstructed from simulated datasets closely resemble the experimental results (Figure 2c), f) and i)). Note that both the experimentally- and theoretically-rendered images

exhibit significant signal decay toward the central area (equator) of the sphere (Figure 2j), green and orange lines). However, these effects are not illumination related and are rather attributed to the limited-view artefact caused by the restricted 140° tomographic coverage of the spherical array detector.[39,35]. Herein, we provide a detailed characterization of the resolution at different points within the FOV. It is shown that the estimated resolution along all directions is generally confined in the 150- 250μm range for a cylindrical field of view of 10 mm length and 10 mm diameter (**Supplemental Figure 4**).

3.2. Tissue Imaging

MIPs of the reconstructed optoacoustic images of the *ex vivo* murine brain and heart are shown in **Figure 3** and **Figure 4**. Both the brain and the heart can be visualised in their entirety with key anatomical structures clearly discernible, including both atria and ventricles as well as the coronary artery in the heart (Figure 3a) and b)).[40-44] In the brain, both right and left cortices, the medulla and the cerebellum are visible along with additional deep seated structures, as labelled (Figure 4a) and b).[45,46] In addition, individual image cross sections taken from both organs (Figure 3c) to e) and 4c) to e)) show that superficial as well as deep structures can be clearly discerned when referenced to widely available atlases [39-45] and gross anatomical images (**Supplemental Figure 3 a) to c)**). The relatively uniform optoacoustic signal and contrast exhibited in the cross-sectional views of the heart and the brain was achieved despite significant light attenuation due to absorption and scattering (Figures 3f) and g) and 4f) and g)), thus clearly evincing the importance of uniform light delivery in volumetric optoacoustic tomography.

4. DISCUSSION AND CONCLUSIONS

In this work, we have demonstrated the implementation of a uniform illumination solution for volumetric optoacoustic tomography and showcased its advantages in tissue-mimicking

phantoms and mouse organs *ex vivo*. The uniform sample illumination was achieved with a custom-designed bundle of multimode optical fibers. The high numerical aperture of the fibers obtains high signal to noise ratio with single-shot excitations while efficiently covering the entire surface of the imaged sample. The optimum configuration of the fibers was established with ray-tracing-based simulations. It should be noted that whilst further illumination improvements tailored to specific applications may be possible, the current configuration was deemed appropriate for a generally applicable case. The accurate fiber positioning was ensured with a 3D-printed mount designed *ad hoc* for holding the ultrasound transducer and the fiber outputs. The mount was printed using 3D Printing technology from a CAD design and sealed to prevent water leakage during the experiments. Proper water enclosing provides an optimum platform for minimizing light energy loss as well as guaranteeing acoustic coupling of the optoacoustically-excited pressure waves. By availing of the freedom of design afforded by the 3D printing technique, the design could be readily adjusted to a different illumination configuration, size and orientation of the detection array, sample location, etc.

The enhancement in imaging performance was quantified using a spherical object having uniform absorption. When the sphere was uniformly illuminated, its entire surface became visible with the reconstructed images, accurately resembling the theoretically predicted (simulated) values. Even though it has been shown that optoacoustic images can in principle be corrected for non-uniform illumination and light attenuation, it was not necessary in this case.[25, 47,48, 49,50] Such correction for limited-view conditions or for a relatively low number of measuring positions can be still hampered by streak-type artefacts associated with strong non-uniformity of the excitation light field (hot spots).[51] Besides sub-optimal light delivery, which is known to greatly affect quantification in optoacoustic imaging and tomography,[52] the reconstruction accuracy may also be conditioned by other factors, such

as limited coverage of the tomographic detection geometry.[35] Indeed, the incomplete (140°) tomographic coverage of the spherical matrix array was responsible for the image distortions in the central part of the reconstructed sphere, irrespective of the light illumination uniformity. Quantification can also be hampered by acoustic attenuation and scattering in the object. Further challenges for quantification are related to the final-sized aperture and narrow frequency response of the ultrasound sensors, which may result in signal decay at deeper regions, signal broadening and resolution degradation.[37,53,54 ,55,56]

Optimal light delivery can benefit a number of biological applications involving optoacoustic imaging studies as it will improve upon the reconstruction accuracy and capacity for identifying and quantifying presence of biological compounds. One example that was showcased in this work is the imaging of entire extracted tissue samples, such as murine organs. In this way, *in vivo* imaging results could be corroborated in intact blood-free samples *ex vivo* using the same type of contrast and particularly concerning gross external and internal anatomical heart and brain structures, may remove the need for time-consuming histology.[57] Some isolation techniques, such as isolated brain [22] or Langendorff heart preparations,[58,59] enable preserving the organ functionality after extraction and thus could potentially benefit from the improved illumination design suggested in our work. Herein it was shown that murine hearts and brains, when cleared from blood and fixed in PFA can be imaged in their entirety with a single laser pulse. The same imaging strategy could be applied to malignant masses dissected from patients.[13] Homogenous illumination is also key in achieving artefact-free 3D and 4D imaging of behaving small organisms, such as freely-swimming zebrafish larvae [20]. Our approach can effectively enhance the FOV and hence the region where fish motion can be tracked in three dimensions. Optimal light delivery can further facilitate more accurate identification and quantification of bio-marker distribution in tumors visualized with volumetric optoacoustic tomography.[60,61] Homogenous light

delivery would also aid functional studies which rely upon spectral unmixing in multi-spectral optoacoustic tomography (MSOT). The main advantage of the current system is its ability to achieve high spatiotemporal resolution (max isotropic resolution of 150 μm at 100Hz). Future developments could see the system be adapted not only for imaging isolated organs but potentially also for whole-body small animal imaging with a single laser pulse. This would however certainly necessitate development of a dedicated detection array matching the geometry of the entire imaged object. Alternatively, previous studies have rotated the detector with a single illumination fiber around the animal to acquire tomographic whole-body data or translated a ring-shaped transducer array along the entire mouse.[62,63]

In conclusion, optimum light delivery can significantly enhance the effective FOV, quantitativeness and overall performance of volumetric optoacoustic tomography. Considering the unique spatio-temporal resolution range covered with the imaging system employed in the current work,[5] the suggested approach can facilitate more accurate interpretation of OA images in numerous *ex vivo*, *in vivo* and *in vitro* studies, especially when it comes to functional imaging studies where more homogenous light delivery could result in more accurate spectral unmixing and quantification of specific chromophores.[64]

Acknowledgements

This study was supported by the European Research Council Consolidator grant ERC-2015-CoG-682379.

REFERENCES

[1] J. Xia, J. Yao, L. V. Wang *Electromagnetic waves (Cambridge, Mass.)*. **2014**, *147*, 1-22.
[2] J. Xia, L. V. Wang *IEEE transactions on bio-medical engineering*. **2014**, *61*, 1380-1389.
[3] P. Beard *Interface Focus*. **2011**, *1*, 602-631.
[4] L. H. V. Wang, S. Hu *Science*. **2012**, *335*, 1458-1462.
[5] X. L. Dean-Ben, S. Gottschalk, B. Mc Larney, S. Shoham, D. Razansky *Chem Soc Rev*. **2017**, *46*, 2158-2198.
[6] L. Li, J. Xia, G. Li, A. Garcia-Uribe, Q. Sheng, M. A. Anastasio, L. V. Wang *Neurophotonics*. **2016**, *3*, 035001.
[7] K. Kim, H. Park, K. M. Lim *Toxicol Res*. **2015**, *31*, 97-104.
[8] P. P. Laissue, R. A. Alghamdi, P. Tomancak, E. G. Reynaud, H. Shroff *Nat Methods*. **2017**, *14*, 657-661.
[9] L. V. Wang, J. Yao *Nat Methods*. **2016**, *13*, 627-638.
[10] A. Taruttis, V. Ntziachristos *Nat Photonics*. **2015**, *9*, 219-227.
[11] A. Dima, V. Ntziachristos *Photoacoustics*. **2016**, *4*, 65-69.
[12] V. Neuschmelting, N. C. Burton, H. Lockau, A. Urich, S. Harmsen, V. Ntziachristos, M. F. Kircher *Photoacoustics*. **2016**, *4*, 1-10.
[13] I. Stoffels, S. Morscher, I. Helfrich, U. Hillen, J. Leyh, N. C. Burton, T. C. Sardella, J. Claussen, T. D. Poeppel, H. S. Bachmann, A. Roesch, K. Griewank, D. Schadendorf, M. Gunzer, J. Klode *Sci Transl Med*. **2015**, *7*, 317ra199.
[14] G. Diot, S. Metz, A. Noske, E. Liapis, B. Schroeder, S. V. Ovsepian, R. Meier, E. Rummeny, V. Ntziachristos *Clin Cancer Res*. **2017**, *23*, 6912-6922.
[15] J. Reber, M. Willershauser, A. Karlas, K. Paul-Yuan, G. Diot, D. Franz, T. Fromme, S. V. Ovsepian, N. Beziere, E. Dubikovskaya, D. C. Karampinos, C. Holzapfel, H. Hauner, M. Klingenspor, V. Ntziachristos *Cell Metab*. **2018**, *27*, 689-+.
[16] F. T. Felix, D. B. X. Luís, S. Peter, S. Ronald, R. Daniel *Journal of Biophotonics*. **2016**, *9*, 934-941.
[17] L. Xiang, B. Wang, L. Ji, H. Jiang *Scientific reports*. **2013**, *3*, 1113.
[18] S. Gottschalk, T. F. Fehm, X. L. Dean-Ben, D. Razansky *J Cerebr Blood F Met*. **2015**, *35*, 531-535.
[19] S. Gottschalk, T. F. Fehm, X. L. Deán-Ben, V. Tsytsarev, D. Razansky *Neurophotonics*. **2016**, *4*, 011007.
[20] X. L. Dean-Ben, H. Lopez-Schier, D. Razansky *Scientific Reports*. **2017**, *7*.
[21] A. ÖZBEK, X. L. DEÁN-BEN, D. RAZANSKY *Optica*. **2018**, *in press*.
[22] X. L. Dean-Ben, G. Sela, A. Lauri, M. Kneipp, V. Ntziachristos, G. G. Westmeyer, S. Shoham, D. Razansky *Light-Sci Appl*. **2016**, *5*.
[23] L. Lin, J. Xia, T. T. W. Wong, L. Li, L. V. Wang *J Biomed Opt*. **2015**, *20*.
[24] M. Omar, J. Rebling, K. Wicker, T. Schmitt-Manderbach, M. Schwarz, J. Gateau, H. Lopez-Schier, T. Mappes, V. Ntziachristos *Light-Sci Appl*. **2017**, *6*.
[25] K. G. Held, M. Jaeger, J. Rička, M. Frenz, H. G. Akarçay *Photoacoustics*. **2016**, *4*, 70-80.
[26] C. W. Hupple, S. Morscher, N. C. Burton, M. D. Pagel, L. R. McNally, J. Cárdenas-Rodríguez *Photoacoustics*. **2018**, *10*, 54-64.
[27] J. Gateau, T. Chaigne, O. Katz, S. Gigan, E. Bossy *Opt Lett*. **2013**, *38*, 5188-5191.
[28] W. F. Xia, D. Piras, M. K. A. Singh, J. C. G. van Hespen, T. G. van Leeuwen, W. Steenbergen, S. Manohar *Biomed. Opt. Express*. **2013**, *4*, 2555-2569.
[29] D. A. Krohn, B. P. McCann in Silica optical fibers: technology update, Vol. 2396 (Ed.^Eds.: Editor), SPIE, City, **1995**, pp.10.
[30] S. Royer, B. V. Zemelman, M. Barbic, A. Losonczy, G. Buzsaki, J. C. Magee *Eur J Neurosci*. **2010**, *31*, 2279-2291.
[31] X. L. Dean-Ben, A. Ozbek, D. Razansky *IEEE Trans Med Imaging*. **2013**, *32*, 2050-2055.

[32] W.-F. Cheong, S. A. Prahl, A. J. Welch *IEEE journal of quantum electronics*. **1990**, *26*, 2166-2185.
[33] P. Lai, X. Xu, L. V. Wang *J Biomed Opt*. **2014**, *19*, 35002.
[34] A. Ozbek, X. Deán-Ben, D. Razansky in Realtime parallel back-projection algorithm for three-dimensional optoacoustic imaging devices, Vol. (Ed.^Eds.: Editor), Optical Society of America, City, **2013**, pp.88000I.
[35] X. L. Deán-Ben, D. Razansky *Photoacoustics*. **2016**, *4*, 133-140.
[36] L. Ding, X. L. Dean-Ben, D. Razansky *IEEE Trans Med Imaging*. **2017**, *36*, 1858-1867.
[37] D. Queiros, X. L. Dean-Ben, A. Buehler, D. Razansky, A. Rosenthal, V. Ntziachristos *J Biomed Opt*. **2013**, *18*, 076014.
[38] G. J. Gage, D. R. Kipke, W. Shain *J Vis Exp*. **2012**.
[39] Y. Xu, L. V. Wang, G. Ambartsoumian, P. Kuchment *Med Phys*. **2004**, *31*, 724-733.
[40] C. Dullin, R. Ufartes, E. Larsson, S. Martin, M. Lazzarini, G. Tromba, J. Missbach-Guentner, D. Pinkert-Leetsch, D. M. Katschinski, F. Alves *PLOS ONE*. **2017**, *12*, e0170597.
[41] C. T. Badea, B. Fubara, L. W. Hedlund, G. A. Johnson *Molecular Imaging*. **2005**, *4*, 15353500200504187.
[42] A. N. Tullio, D. Accili, V. J. Ferrans, Z.-X. Yu, K. Takeda, A. Grinberg, H. Westphal, Y. A. Preston, R. S. Adelstein *Proceedings of the National Academy of Sciences*. **1997**, *94*, 12407-12412.
[43] A. Yoldas, E. Ozmen, V. Ozdemir *Journal of the South African Veterinary Association*. **2010**, *81*, 247-252.
[44] I. Takamasa, Y. Hiroshi, H. Toshiyuki *Braintree Scientific*. **2001**.
[45] S. W. Oh, J. A. Harris, L. Ng, B. Winslow, N. Cain, S. Mihalas, Q. Wang, C. Lau, L. Kuan, A. M. Henry, M. T. Mortrud, B. Ouellette, T. N. Nguyen, S. A. Sorensen, C. R. Slaughterbeck, W. Wakeman, Y. Li, D. Feng, A. Ho, E. Nicholas, K. E. Hirokawa, P. Bohn, K. M. Joines, H. Peng, M. J. Hawrylycz, J. W. Phillips, J. G. Hohmann, P. Wohnoutka, C. R. Gerfen, C. Koch, A. Bernard, C. Dang, A. R. Jones, H. Zeng *Nature*. **2014**, *508*, 207.
[46] E. S. Lein, M. J. Hawrylycz, N. Ao, M. Ayres, A. Bensinger, A. Bernard, A. F. Boe, M. S. Boguski, K. S. Brockway, E. J. Byrnes, L. Chen, L. Chen, T.-M. Chen, M. Chi Chin, J. Chong, B. E. Crook, A. Czaplinska, C. N. Dang, S. Datta, N. R. Dee, A. L. Desaki, T. Desta, E. Diep, T. A. Dolbeare, M. J. Donelan, H.-W. Dong, J. G. Dougherty, B. J. Duncan, A. J. Ebbert, G. Eichele, L. K. Estin, C. Faber, B. A. Facer, R. Fields, S. R. Fischer, T. P. Fliss, C. Frensley, S. N. Gates, K. J. Glattfelder, K. R. Halverson, M. R. Hart, J. G. Hohmann, M. P. Howell, D. P. Jeung, R. A. Johnson, P. T. Karr, R. Kawal, J. M. Kidney, R. H. Knapik, C. L. Kuan, J. H. Lake, A. R. Laramee, K. D. Larsen, C. Lau, T. A. Lemon, A. J. Liang, Y. Liu, L. T. Luong, J. Michaels, J. J. Morgan, R. J. Morgan, M. T. Mortrud, N. F. Mosqueda, L. L. Ng, R. Ng, G. J. Orta, C. C. Overly, T. H. Pak, S. E. Parry, S. D. Pathak, O. C. Pearson, R. B. Puchalski, Z. L. Riley, H. R. Rockett, S. A. Rowland, J. J. Royall, M. J. Ruiz, N. R. Sarno, K. Schaffnit, N. V. Shapovalova, T. Sivisay, C. R. Slaughterbeck, S. C. Smith, K. A. Smith, B. I. Smith, A. J. Sodt, N. N. Stewart, K.-R. Stumpf, S. M. Sunkin, M. Sutram, A. Tam, C. D. Teemer, C. Thaller, C. L. Thompson, L. R. Varnam, A. Visel, R. M. Whitlock, P. E. Wohnoutka, C. K. Wolkey, V. Y. Wong, M. Wood, M. B. Yaylaoglu, R. C. Young, B. L. Youngstrom, X. Feng Yuan, B. Zhang, T. A. Zwingman, A. R. Jones *Nature*. **2006**, *445*, 168.
[47] A. Q. Bauer, R. E. Nothdurft, J. P. Culver, T. N. Erpelding, L. V. Wang *J Biomed Opt*. **2011**, *16*, 096016.
[48] T. Harrison, P. Shao, R. J. Zemp *Biomed. Opt. Express*. **2013**, *4*, 2224-2230.
[49] M. Kirillin, V. Perekatova, I. Turchin, P. Subochev *Photoacoustics*. **2017**, *8*, 59-67.
[50] X. L. Deán-Ben, A. C. Stiel, Y. Jiang, V. Ntziachristos, G. G. Westmeyer, D. Razansky *Opt Lett*. **2015**, *40*, 4691-4694.
[51] G. Paltauf, R. Nuster, P. Burgholzer *Physics in Medicine and Biology*. **2009**, *54*, 3303-3314.
[52] B. Cox, J. G. Laufer, S. R. Arridge, P. C. Beard *J Biomed Opt*. **2012**, *17*.
[53] X. L. Dean-Ben, D. Razansky, V. Ntziachristos *Physics in Medicine and Biology*. **2011**, *56*, 6129-6148.
[54] N. Baddour, A. Mandelis *Photoacoustics*. **2015**, *3*, 132-142.

[55] E. Filoux, J. Mamou, O. Aristizábal, J. A. Ketterling *IEEE transactions on ultrasonics, ferroelectrics, and frequency control*. **2011**, *58*.
[56] H. K. Zhang, A. Cheng, N. Bottenus, X. Guo, G. E. Trahey, E. M. Boctor *Journal of Medical Imaging*. **2016**, *3*, 027001.
[57] J. W. McGowan, G. L. Bidwell III *Journal of visualized experiments: JoVE*. **2016**.
[58] R. M. Bell, M. M. Mocanu, D. M. Yellon *J Mol Cell Cardiol*. **2011**, *50*, 940-950.
[59] D. Lang, M. Sulkin, Q. Lou, I. R. Efimov *Jove-J Vis Exp*. **2011**.
[60] L. Kirscher, X. L. Dean-Ben, M. Scadeng, A. Zaremba, Q. Zhang, C. Kober, T. F. Fehm, D. Razansky, V. Ntziachristos, J. Stritzker, A. A. Szalay *Theranostics*. **2015**, *5*, 1045-1057.
[61] V. Ermolayev, X. L. Dean-Ben, S. Mandal, V. Ntziachristos, D. Razansky *Eur Radiol*. **2016**, *26*, 1843-1851.
[62] X. L. Deán-Ben, T. F. Fehm, S. J. Ford, S. Gottschalk, D. Razansky *Light: Science &Amp; Applications*. **2017**, *6*, e16247.
[63] A. Taruttis, S. Morscher, N. C. Burton, D. Razansky, V. Ntziachristos *PLOS ONE*. **2012**, *7*, e30491.
[64] X. Luís Deán-Ben, D. Razansky *Light: Science &Amp; Applications*. **2014**, *3*, e137.

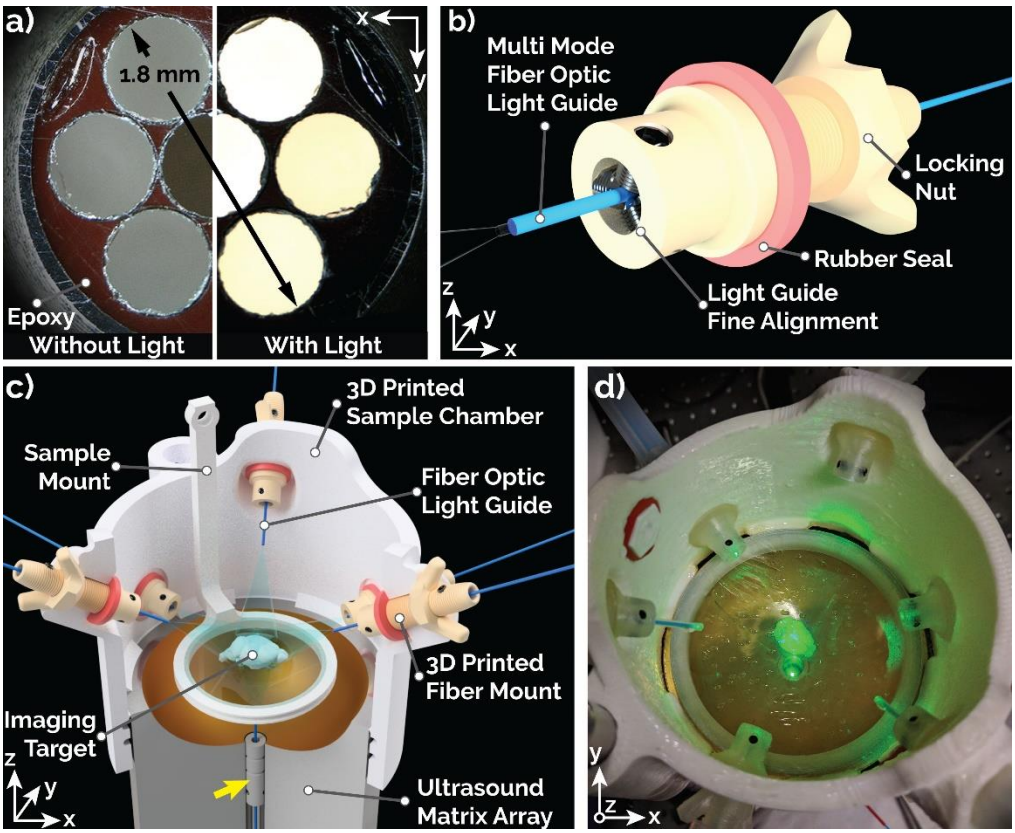

Figure 1. a) Fabricated and polished fiber bundle (coupling end) with a final diameter of 1.8 mm. It is comprised of seven 600 µm multimode glass fibers. b) Enlarged rendering view of the fiber mount including seals, alignment bolts and the fiber itself. c) Inventor rendering of the assembly of the entire holder, ultrasound matrix array transducer and the imaged sample. The yellow arrow indicates the single fiber used for single side illumination. For uniform illumination all 7 fibers were used. d) Colour photograph of the printed, sealed and assembled 3D-printed holder accommodating the transducer.

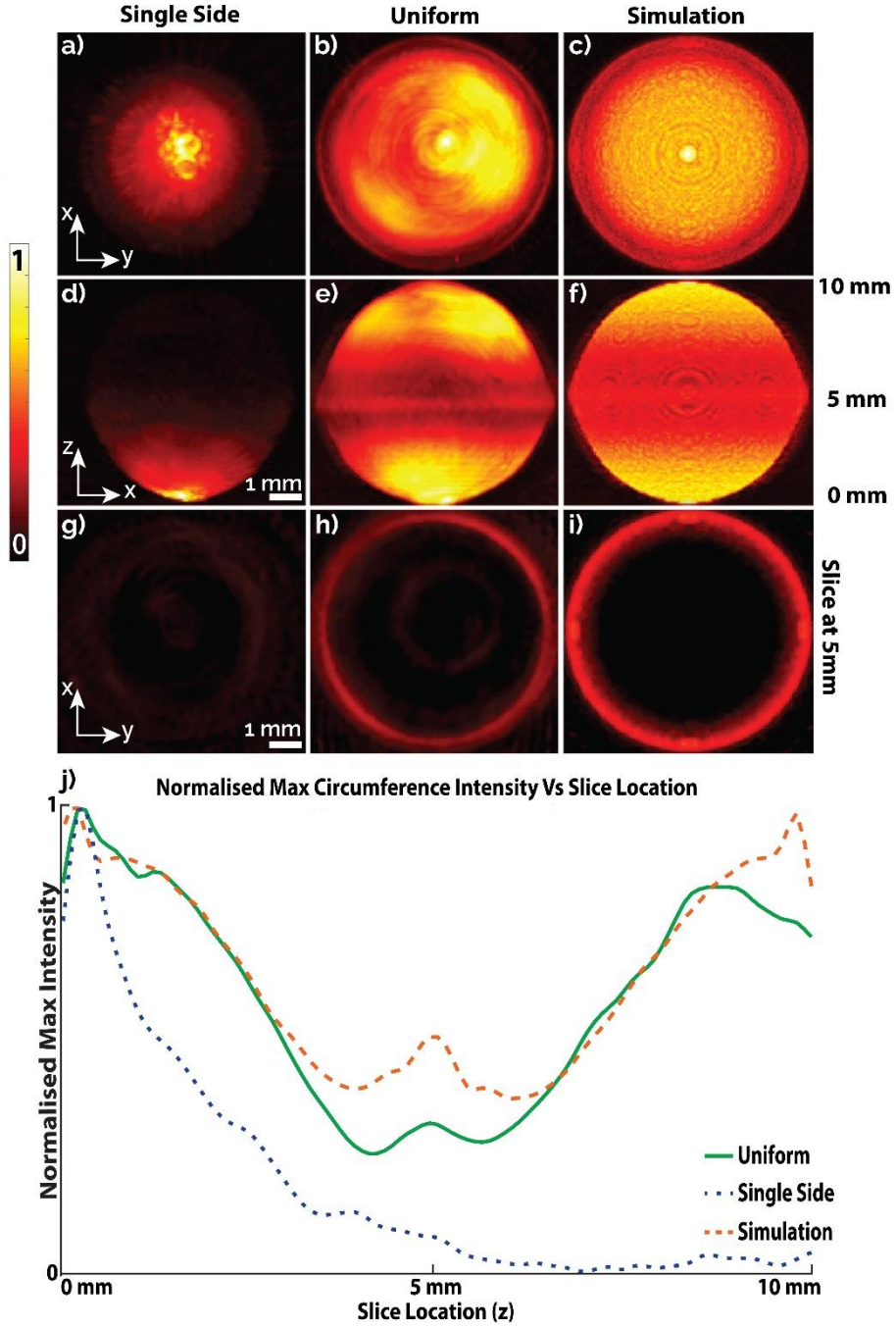

Figure 2. Comparison between experimental and simulated volumetric optoacoustic reconstructions. (a)-(c) Maximal intensity (MIP) projection images looking from the top of each sphere for the single side, uniform and simulated (perfect) illumination scenarios, respectively. (d)-(f) The corresponding side view MIPs. (g)-(i) Single cross-sectional slices through the centre of each sphere. (j) Max circumference signal intensity in each Z slice of the respective spheres.

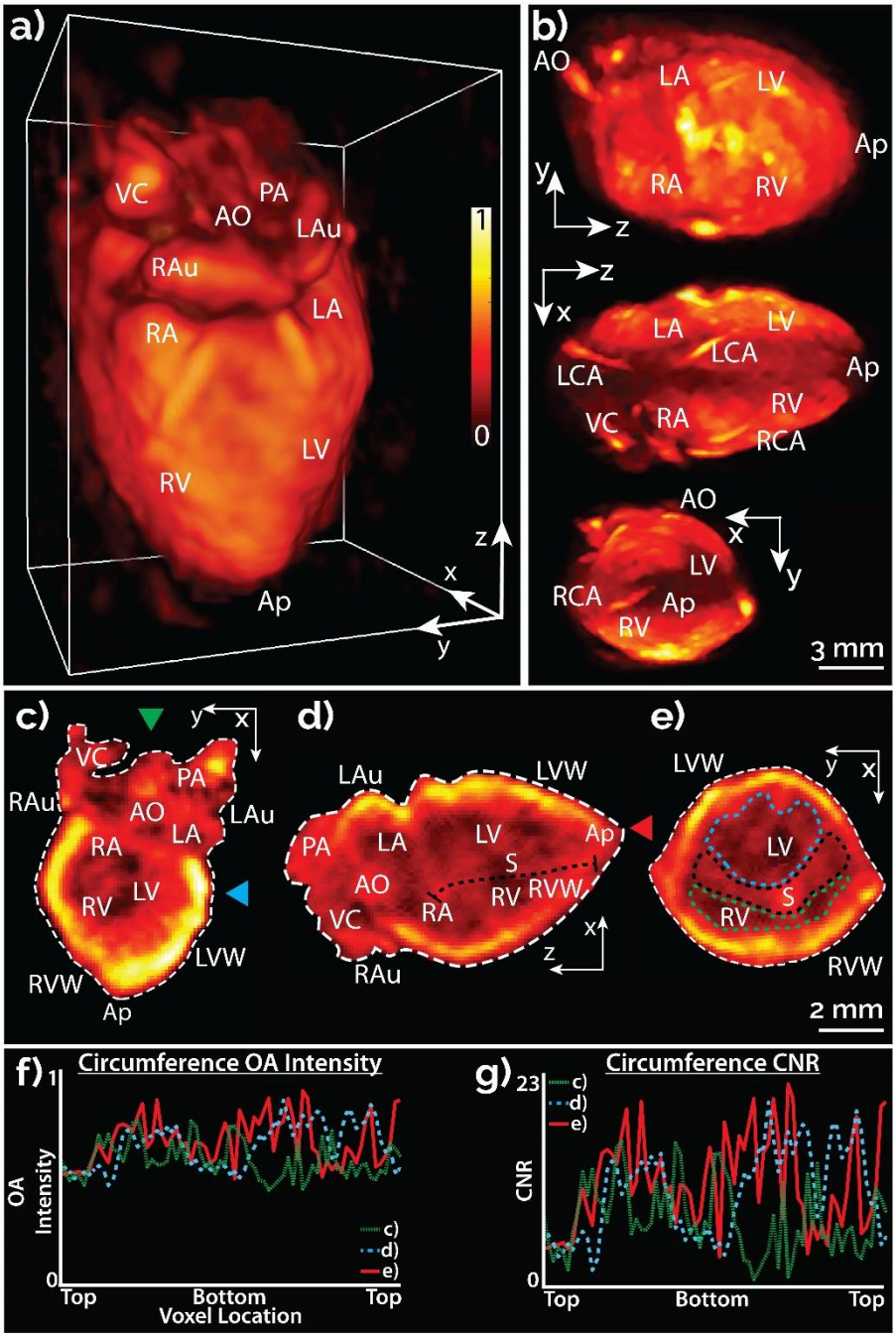

Figure 3. Validation of the uniform light delivery approach in an ex vivo murine heart. (a) Volumetric optoacoustic tomography rendering from an excised murine heart. (b) MIP views along the coronal, sagittal and transverse views are shown. (c,d,e) The corresponding coronal, sagittal and transverse orthoslices of the murine heart. The green arrow shows the slice location for d), the blue arrow for e) and red arrow for c). Indications of gross anatomical structures are labelled. AO: Aorta, VC: Vena Cava, LA: Left Atrium, LV: Left Ventricle, LVW: Left Ventricular Wall, RA: Right Atrium, RV: Right Ventricle, RVW: Right Ventricular Wall, Ap: Apex, LAu: Left Auricle, RAu: Right Auricle, S: Septum, LCA: Left Coronary Artery, RCA: Right Coronary Artery. The black line highlights the septum. f) OA circumference intensity values for corresponding sectional views as listed. g) Corresponding contrast-to-noise ratios (CNR) for the voxels shown in f).

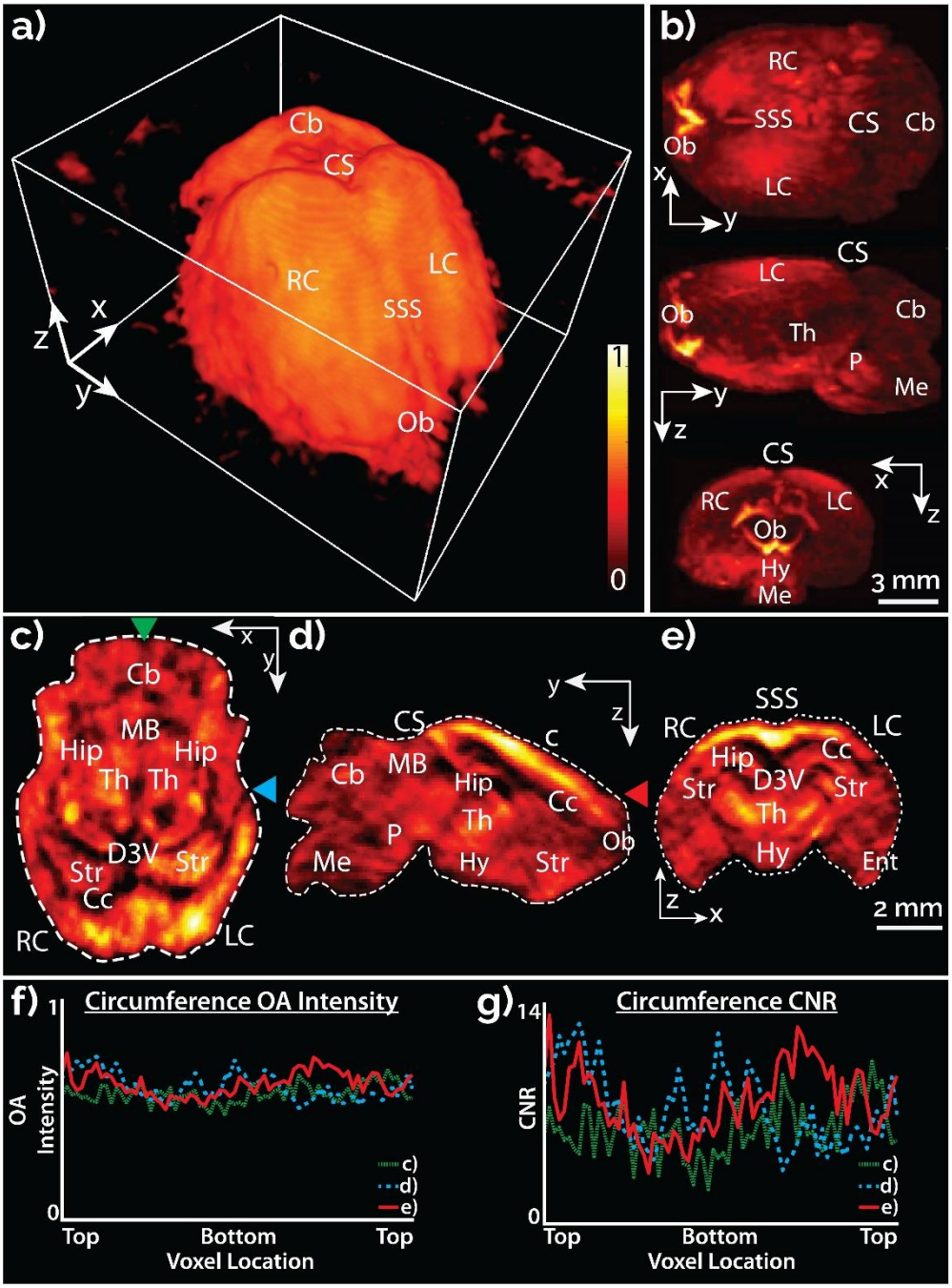

Figure 4. Validation of the uniform light delivery approach in an ex vivo murine brain. (a) Volumetric optoacoustic tomography rendering from an excised murine brain. (b) MIP views along the coronal, sagittal and transverse views are shown. (c,d,e) The corresponding coronal, sagittal and transverse orthoslices of the murine brain are shown. The green arrow shows the slice location for d), the blue arrow for e) and red arrow for c). Indications of gross anatomical structures are labelled. Ob: Olfactory bulbs, SSS: Superior Sagittal Sinus, RC: Right Cortex, LC: Left Cortex, Cb: Cerebellum, Th: Thalamus, P: Pons, Me: Medulla, Hy: Hypothalamus, Hip: Hippocampus, D3V: Dorsal Third Ventricle, Th: Thalamus, , RV: Right Ventricle, LV: Left Ventricle, Ent: Entorhinal Cortex, Str: Striatum, CS: Confluence of Sinuses, MB: Mid-Brain f) OA circumference intensity values for corresponding sectional views as listed. g) Corresponding contrast-to-noise ratios (CNR) for the voxels shown in f).